# Effect of Surfactant on Electrochemically Generated Surface Nanobubbles

Milomir Suvira and Bo Zhang*
Department of Chemistry, University of Washington, Seattle, WA 98195-1700 United States

Corresponding author, email: zhangb@uw.edu

Phone: 1-206-543-1767
Fax: 1-206-685-8665

**Abstract.** Surfactants, mimics of contamination, play an important role in nanobubble nucleation, stability, and growth at the electrode surface. Herein, we utilize single-molecule fluorescence microscopy as a sensitive imaging tool to monitor nanobubble dynamics in the presence of surfactant. Our results show that the presence of anionic and non-ionic surfactant increases the rate of nanobubble nucleation at all potentials in a voltage scan. The fluorescence and electrochemical responses indicate the successful lowering of the critical gas concentration needed for nanobubble nucleation across all voltages. Furthermore, we demonstrate that the accumulation of surfactants at the gas-liquid interface changes the interaction of fluorophores with the nanobubble surface. Specifically, differences in fluorophore intensity and residence lifetime at the nanobubble surface suggest that the labeling of nanobubbles is affected by the nature of the nanobubble (size, shape, etc.) and the structure of the gas-liquid interface (surfactant charge, hydrophobicity, etc.).

**Introduction.** Gases are produced in many energy-related electrochemical processes. Some of these gas products offer a "green" fuel source for cleaner and sustainable alternatives to meet the energy demands of our society. For example, in water electrolysis, water is oxidized on the anode while simultaneously being reduced on the cathode, producing energetically rich $O_2$ and $H_2$ gas, respectively.[1] $N_2$ and $CO_2$ gases are produced in hydrazine and formate fuel cells.[2,3] However, the rapid evolution of gas molecules and their comparatively slow diffusion from the electrode surface can create a supersaturated gas environment favorable for nanobubble formation.[4] The nucleation, growth, and dissolution/detachment of surface nanobubbles may affect electrochemical reactions for a number of reasons: reduced electrocatalytic surface,[5] reorganization of the diffusion layer,[6] and increased ohmic and mass-transfer resistances.[7] An excellent review that details the impacts of electrochemically generated gas bubbles has been published recently.[8] Nonetheless, many observed phenomena remain unexplained or inconclusive. Expanding our understanding of the unique properties of electrochemically generated surface nanobubbles is critical to further advance technologies related to energy generation and consumption.

The stability of surface nanobubbles has perplexed researchers for decades due to their high internal pressures[9] and long lifetimes.[10] Of all the numerous explanations that have been proposed, there are three major theories for the nanobubble stability, which include contact line pinning,[11] dynamic equilibrium,[12] and gas-liquid interface stabilization by contaminants.[13] Contamination theory proposes that a thin organic layer at the gas-liquid interface stabilizes the nanobubble due to a reduction in the gas-liquid surface tension. A reduction in the gas-liquid surface tension also leads to a reduction in the Laplace pressure.[9,14] The reduced nanobubble pressure ensures that the bubble remains at the substrate surface. An alternative explanation is that an organic-like layer hinders the influx and outflux of gas molecules to prolong the nanobubble lifetime indefinitely.[13] Interestingly, White and co-workers reported that surfactants, mimics of contamination, lower the surface gas concentration needed to nucleate a bubble on the surface of a metal nanoelectrode.[15] We were inspired by their work as our previous studies demonstrated that nanobubbles can nucleate well before the thermodynamic potential required for $H_2$ and

$O_2$ production.[16,17] We hypothesized that the voltage needed to nucleate a nanobubble could further be shifted if the critical gas concentration is lowered in the presence of added surfactant molecules.

Surface nanobubbles have been studied by a wide range of techniques including atomic force microscopy (AFM),[18] dark-field microscopy[19], surface-plasmon resonance and electrochemistry.[20] Ohl and coworkers introduced a total-internal reflection fluorescence (TIRF) microscopy technique to image nanobubble formation during solvent exchange.[21] This technique was recently used by the Wang group to study photocatalytic activity of single CdS nanoparticles by imaging the $H_2$ nanobubbles on their surfaces.[22] Our group expanded on the method by using single fluorophores to label electrochemically generated $H_2$ nanobubbles.[16] The super-resolution approach enables the monitoring of nanobubble nucleation and growth with high temporal and spatial resolution. Highly-sensitive optical based detections are advantageous in monitoring gas nucleation as experiments and theoretical calculations estimate that only 30 to 50 gas molecules are needed for heterogeneous nanobubble nucleation.[23,24] Under these circumstances, it could be extremely difficult, if not impossible, to measure any detectable current fluctuations during the initial gas nucleus formation. Understanding the initial nucleation step before the bubble grows is technologically and fundamentally relevant.

In this work, we use single-molecule TIRF microscopy to show that the presence of surfactant promotes earlier nanobubble nucleation. We observe an increase in nanobubble generation at all voltages where nanobubbles are detected. Furthermore, we demonstrate that shrinking nanobubbles remain on the surface of the electrode at potentials where dissolution is increasingly more likely. Lastly, the accumulation of surfactant at the gas-liquid interface changes the labeling fluorophore intensity and residence time at the nanobubble surface.

## Experimental Section

*Chemicals:* Rhodamine 6G (R6G) perchlorate (Kodak), sodium sulfate (J.T. Baker), isopropyl alcohol (Fisher Chemical, sodium dodecyl sulfate (SDS) (Aldrich), indium-tin-oxide (ITO) coated coverslips (SPI

Supplies), triton X-100  (TX-100) (Aldrich) assume 625 g/mol for concentration calculations. All solutions were made using deionized water (>18 MΩ•cm).

*TIRF Microscopy:* TIRF microscopy was performed using a home-built inverted microscope (Olympus IX70). An Olympus Apo N 60X 1.49 NA oil objective and an additional 1.5X magnification was used for all imaging experiments. A 532 nm green laser (10 mW) was used as the excitation source (CrystaLaser). Light was filtered with an ET590/50m emission filter (Chroma Technology) before being detected by an Andor iXon+ EMCCD camera. Images were recorded at an exposure time of 50 ms (19.81 Hz). An amplifier gain of 300 and preamplifier gain of 5.1 were used in all experiments. A 6 μL droplet of solution containing 100 pM R6G, 1M $Na_2SO_4$, and varying concentrations of SDS and TX-100 were placed on a 2 mm diameter hole in a polydimethylsiloxane (PDMS) film defining the ITO working electrode. In the nanobubble experiments, a voltage waveform (0 to -2 to 0 V vs Pt QRE @ 100 mV/s) was applied using a 273A potentiostat (Princeton Applied Research) to an ITO working electrode using a Pt wire as a quasi-reference electrode. In constant potential experiments, the voltage was held at -1 V vs Pt QRE while imaging nanobubble fluorophore labeling for 3000 frames (~2.5 minutes). A PCI-6251 (National Instruments) data acquisition card and a BNC-2090 breakout box were used to interface the potentiostat with the computer. Finally, a traditional 3-electrode configuration was used to record the current-voltage response of a Pt wire in 0.5 M $H_2SO_4$ during a CV scan (-0.69 to 0.9 to -0.69 V vs Hg/HgSO4 @ 100 mV/s). A 1 mm diameter Pt wire (~1 cm length) was used as the working electrode, a Pt wire as the counter electrode, and a $Hg/HgSO_4$ electrode (CH Instruments, Inc.) as the reference.

*Image Analysis:* Images of single molecule labeling of nanobubbles were first background subtracted using a rolling ball radius of 5 pixels in ImageJ. All images were adjusted to have the same brightness and contrast before further analysis. The ThunderSTORM plugin in ImageJ was used to detect spots deemed to be nanobubbles.[25] Each spot can be described by a point spread function which can be fitted using a 2D gaussian function. A peak intensity threshold 1.25 times the standard deviation of the wavelet filter was used. Intensity from each individual spot is extracted by integrating under the fitted Gaussian curve.

*Single-Molecule Tracking*: The TrackMate plugin in ImageJ was used for "spot" tracking.[26] A Laplacian

of a Gaussian detector is used to define detect spots above a user set threshold. Once spots have been

identified, a simple LAP tracker is used to track the duration of the detected spot. The linking and gap-

closing distance was set to 300 nm. A gap-closing max frame gap of 3 frames was used. The duration of

events was obtained, and a histogram was created. The histogram was fit using a single exponential decay
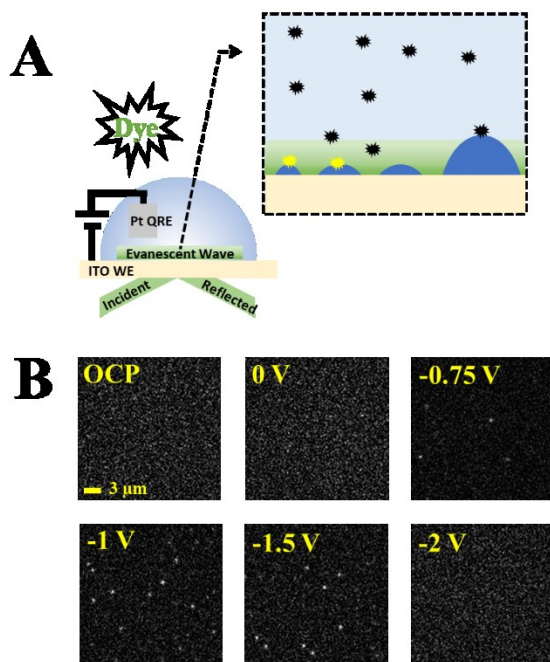
function in Origin in order to extract tau, $\tau$.



**Figure 1:** Total-internal reflection fluorescence microscopy as a tool to image $H_2$ nanobubbles. **A)** Experimental setup showing $H_2$ nanobubble generation and dye labeling at an ITO working electrode. **B)** A series of six fluorescence images obtained in constant potential experiments showing nanobubble labeling (or lack thereof) at open circuit potential (OCP), 0, -0.75, -1, -1.5, and -2 V vs Pt QRE. The solution contained 100 pM R6G and 1 M $Na_2SO_4$.

**Results and Discussion**

*Effect of SDS on Nanobubble Formation.* The thermodynamic potential for electrochemical water

splitting is 1.23 V. In electrochemical water splitting, water is reduced on the cathode ($2H_2O + 2e^- \rightarrow H_2$

$_{(g)} + 2OH^-$) while simultaneously being oxidized ($2H_2O \rightarrow 4H^+ + 4e^- + O_2$ $_{(g)}$) on the anode. Gaseous $H_2$ or

$O_2$ molecules begin to evolve at both the cathode and anode, respectively. At or above certain critical gas

concentration, a nanobubble nucleates on the electrode surface heterogeneously.[23] **Figure 1A** shows the experimental setup used to generate and optically detect nanobubble nucleation and growth. Briefly, an objective-based total-internal reflection fluorescence (TIRF) microscope is used to produce a decaying evanescent wave at the surface of an indium-tin-oxide (ITO) working electrode. A Pt wire acts as a quasi-reference electrode (QRE). Two of the most probable reactions on the Pt wire QRE are the oxidation of Pt itself to form Pt oxide and the water oxidation. As shown in **Figure S1**, the oxidation of Pt starts at ~0.02 V vs Hg/HgSO$_4$ reference electrode or +0.7 V vs NHE, which is ~0.7 V lower than the onset potential of the H$_2$O oxidation wave. Similar to our previous work, we observed early nucleation events for H$_2$ nanobubbles at about -0.75 V vs Pt QRE.[16] Although it is certainly possible that the anodic reaction on Pt QRE was Pt oxidation, in which case, the initial H$_2$ nucleation potential would be around -0.07 V vs NHE. However, it is also known that the oxidation of Pt is limited to the top one or two atomic layers on the surface of the Pt electrode unless potentials >1.5 V vs NHE are reached for an extended time.[27,28,29] As such, it is likely that the primary anodic reaction taking place on the Pt QRE is the oxidation of water. In this case, the -0.75 V potential observed for H$_2$ nucleation would indicate a very early gas nucleation potential for water reduction on ITO compared to its -1.23 V thermodynamic potential. We believe this can be understood because of the following reasons. First, the H$_2$ nanobubbles are in the range of 20-30 nm when they are initially detected, *i.e.*, prior to reaching -1.0 V. At higher negative potentials (e.g., -1.5 to -2.0 V vs Pt QRE), most of them grow to 70-100 nm.[16] Although these bubbles are detected by the highly sensitive single-molecule fluorescence method, the overall reaction rates at these lower negative potentials are far from an appreciable rate for practical water splitting, as one can see from the current-voltage response in **Figure 2C**. Second, although ITO is not among the most active materials for HER, certain catalytically-active defect spots may still be present, which could be responsible for the few H$_2$ nanobubbles observed at the scattered locations on the ITO surface.

The fluorophore rhodamine-6G (R6G) is present in solution at pM concentration. At potentials where H$_2$ nanobubbles are not present (e.g., open circuit potential), R6G molecules rapidly diffuse in and out of the evanescent wave without being detected **(Figure 1B).** The quenching ability of the conductive

ITO surface also prevents detection of R6G.[30] However, in the presence of a nanobubble, the fluorophore momentarily "sticks" to the nanobubble surface giving a short fluorescence burst that produces well resolved spots **(Figure 1B)**. Applying greater reducing potentials (e.g., -2V) leads to further nanobubble growth that exceeds the penetration depth of the decaying evanescent wave (~200 nm).[16] Hence, the number of labeled and detected nanobubbles decreases **(Figure 1B)**. Additionally, there are few detections without the presence of dye; these detections are attributable to unavoidable sources of fluorescent contamination **(Figure S2)**.
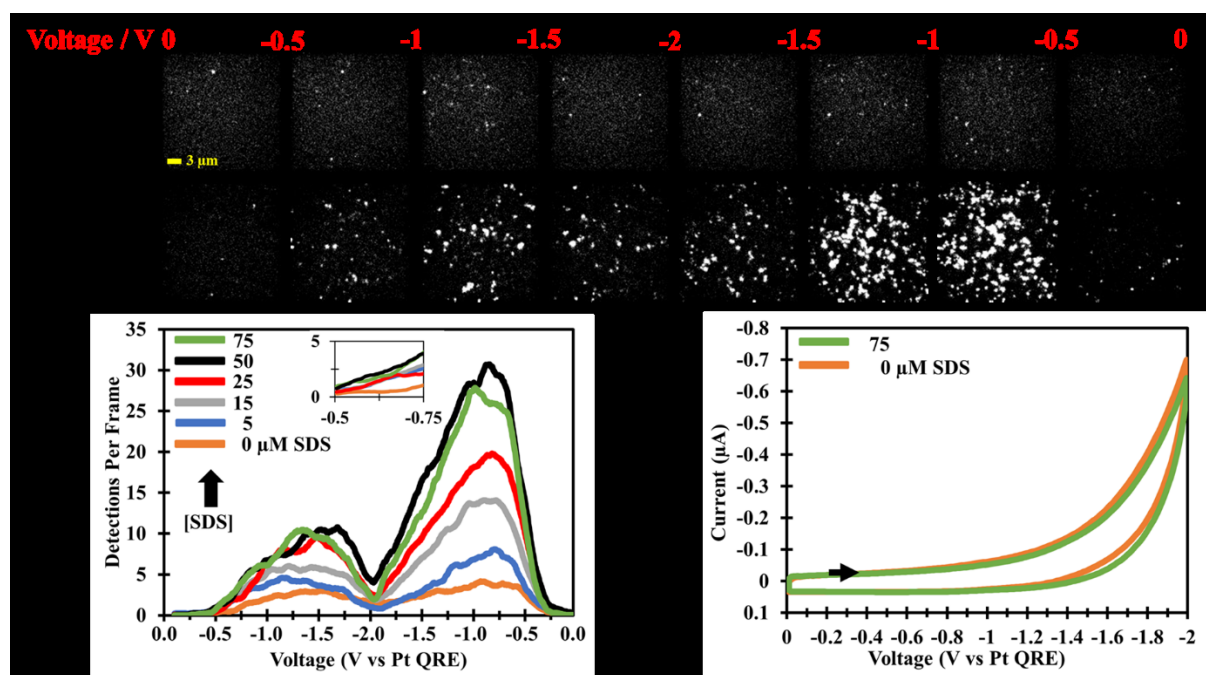


**Figure 2:** Imaging $H_2$ nanobubbles in the presence of SDS. **A)** Summed images (500 mV stack ~100 frames each) extracted from **Video S1**. The potential was scanned from 0 to -2 to 0 V vs Pt QRE at 100 mV/s. The solution contained 100 pM R6G and 1 M $Na_2SO_4$. The testing solution contained 50 μM SDS while the control solution did not. **B)** The moving average (20 frames ~100 mV bin) of nanobubble detections per frame as a function of SDS concentration. N=10 for each condition. **C)** Representative cyclic voltammograms. The solution contained 100 pM R6G, 1 M $Na_2SO_4$, and 0 (75 μM) SDS.

To study the effect of surfactant, we first imaged $H_2$ nanobubbles generated on an ITO electrode during a voltage scan from 0 to -2.0 V in an aqueous solution containing 100 pM R6G, 1 M $Na_2SO_4$, and 50 μM of an anionic surfactant, sodium dodecyl sulfate (SDS). For convenience, **Figure 2A** shows summed images (~ 500 mV stacks taken from **Video S1**) of detected nanobubbles. From the raw data, it is

immediately apparent that there are more nanobubbles being produced and detected in the presence of the SDS (**Video S1**). A concentration dependent study reveals that the amount of nanobubbles produced continues to increase as the SDS concentration increases **(Figure 2B)**. The peak number of nanobubbles detected in the forward and reverse scan is nearly 5 and 15 times greater, respectively, compared to the control. It is important to note that the SDS concentrations used here are well below the critical micelle concentration (CMC), 7-10 mM. [31]

The rate of nucleation for a gaseous surface nanobubble, J ($s^{-1}$), can be described by **Equation 1**.[15,32] C ($s^{-1}$) is a constant, $\gamma$ (N/m) is the liquid surface tension, $\sigma$ is the supersaturation concentration of gas in the liquid, P' (Pa) is the pressure at which nucleation takes place, and $\Phi$ (dimensionless) is a structural parameter that is described by the nanobubble contact angle theta, $\theta$ (degrees) **(Equation 2)**.

$$\mathbf{J = C\ exp\left(\frac{-16\pi\gamma^3\ \Phi(\theta)}{3kT(\sigma P')^2}\right)} \qquad (1)$$

$$\mathbf{\Phi(\theta) = \frac{1}{4}\ (1 + cos\theta)^2(2 - cos\theta)} \qquad (2)$$

It is apparent that even a miniscule decrease to the surface tension, $exp(-\gamma^3)$, could result in a significant increase in the nucleation rate. An increase in the nucleation rate could also correspond to a decrease in the critical electrochemical potential needed to observe nanobubble nucleation. The inset in **Figure 2B** shows more bubbles being labeled and imaged as the surfactant concentration increases within the initial nucleation regime (-0.5 to -0.75 V). This observation indicates the successful increase in the nucleation rate by a lowering of the nanobubble surface tension.

Furthermore, **Figure 2C** shows that the current output during water reduction, within experimental error, is nearly identical with and without the presence of the surfactant SDS. As current is directly proportional to the rate at which $H_2$ gas molecules are produced, the amount of evolved gas at the electrode surface is comparable in the control and surfactant conditions. Hence, the presence of more nanobubbles across all voltages in the optical readout further indicates the successful lowering of the gas concentration needed for nucleation. A similar trend is observed using the non-ionic surfactant Triton X-100 (TX-100) (**Figure 3 and Video S2**). The CMC for TX-100 is 0.22-0.24 mM.[33] This observed

phenomenon is consistent with recent reports that use fluorosurfactant to lower the interfacial gas concentration for nucleation.[20,34]
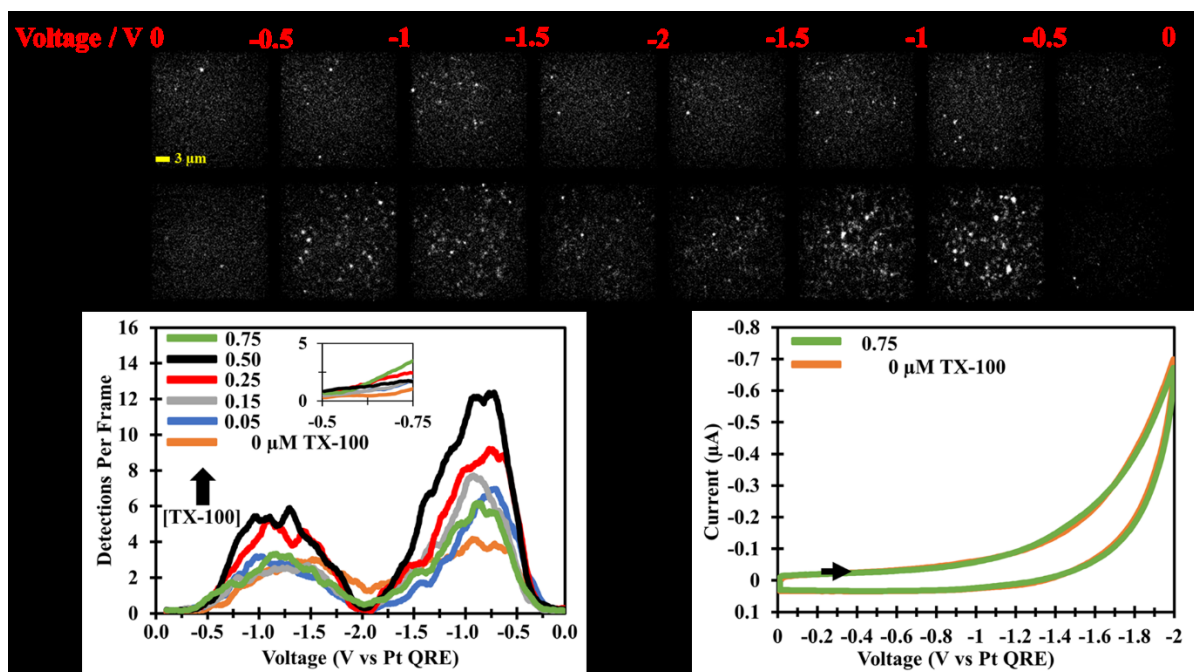


**Figure 3:** Imaging $H_2$ nanobubbles in the presence of TX-100. **A)** Summed images (500 mV stack ~100 frames each) extracted from **Video S2**. The potential was scanned from 0 to -2 to 0 V vs Pt QRE at 100 mV/s. The solution contained 100 pM R6G and 1 M $Na_2SO_4$. The testing solution contained 0.50 μM TX-100 while the control solution did not. **B)** The moving average (20 frames ~100 mV bin) of nanobubble detections per frame as a function of TX-100 concentration. N=10 for each condition. **C)** Representative cyclic voltammograms. The solution contained 100 pM R6G, 1 M $Na_2SO_4$, and 0 (0.75 μM) TX-100.

Classical nucleation theory predicts that the rate of bubble nucleation is highly dependent on the concentration of gas molecules present at the electrode surface. At high surface gas concentrations it becomes thermodynamically favorable for a critical size gas nucleus to grow into a nanobubble.[35] At gas concentrations below some critical value, the rate of nanobubble formation drops precipitously.[36] Nonetheless, we observe nanobubble labeling in potential regions where we do not detect a significant change in the faradaic current. Although catalytic sites on the ITO electrode may contribute to water reduction, it is difficult to justify a high concentration of gas molecules at the electrode surface at the voltages we begin to observe nanobubble labeling. In other words, the fast diffusion of gaseous molecules is presumably more dominant than the production of gas at the electrode surface. Hence, a saturated gaseous environment is unlikely present at the low voltages in the forward scan. Nonetheless, Seddon and

co-workers reported that gas saturation levels are not needed for nanobubble nucleation.[37] Furthermore, a recent simulation study showed that nanobubbles can nucleate in undersaturated conditions if the gas-electrode attraction is greater than the water-electrode attraction.[23] Hydrophobic heterogeneities on the ITO surface may also contribute to the nucleation or preferential adsorption of gas molecules to the electrode surface. Nonetheless, more work is needed to account for this apparent thermodynamic anomaly.

Interestingly, we also observe a large hysteresis in the amount of detected nanobubbles in the reverse scan **(Figure 1B & 2B)**. More specifically, the number of $H_2$ nanobubbles detected on the reverse scan (-2.0 to 0 V) is significantly greater than that detected on the forward scan (0 to -2.0 V). Moreover, this hysteresis is dependent on the surfactant concentration: the more surfactant we had in the solution, the more nanobubbles were detected on the reverse scan. We reason that the hysteresis occurs due to the detection of bubbles from the forward scan and from newly nucleated bubbles in the reverse. The peak number of detections in the forward scan is reached between -1 and -1.5 V for all experiments. After ~ -1.5 V, a drop in detections occurs. The drop in detections in this regime is due to bubbles becoming too big to be effectively detected within the evanescent wave.[16] As the potential is switched towards more positive values in the reverse scan (-2 V → -1.5 V), the outflux of gas molecules begins to outweigh the influx of gas molecules in nanobubbles already present on the electrode surface. Consequently, the bubbles begin to decrease in size and reappear within the evanescent wave. Nevertheless, new nanobubbles are still able to nucleate at these potentials. We are unable to distinguish nanobubbles from the forward and reverse scan.

Finally, a considerable amount of nanobubbles are present in the low voltage regime in the reverse scan (e.g., between -0.75 V and -0.25 V) **(Figure 2B & 3B)**. Bubble growth and shrinkage is influenced by the relative rates of gas outflux and influx at the gas-liquid interface. The rate of gas outflux is difficult to quantify as it is related to the shape, size, and pressure of the nanobubble. However, one of the advantages of generating nanobubbles electrochemically is that the relative concentration of gas molecules at the surface of the electrode can be readily tuned by changing the electrode potential. As

mentioned previously, the amount of $H_2$ gas molecules leaving the nanobubble is presumed to be much greater than the influx of gas into the nanobubble as the voltage becomes more positive, i.e., less driving force for $H_2$ gas evolution. Under these conditions, the bubbles begin to shrink until they completely dissolve or detach from the surface. We hypothesize that the shrinkage of nanobubbles leads to the concentration of surfactant at the gas-liquid interface. The high concentration of organic-like molecules at the interface presumably hinders the outflux of gas molecules and further stabilizes the nanobubble.[13] **Figure S3** shows a simple schematic outlining our hypothesis.

However, others have noted that the permeability of gas molecules is not affected in the presence of soluble surfactant molecules and salts.[38,39] Revisiting gas molecule permeability at a surfactant doped nanobubble surface may be necessary to support our hypothesis. Alternatively, Zhang et al. reported a self-restoring mechanism that ensures nanobubble stability in the presence of contaminants during bubble shrinkage or growth. [40] The theoretical approach does not rely on the hindrance of gas molecules by an organic layer.

*Effect of Surfactant Type on Nanobubble Formation.* To further understand how different surfactants may affect nanobubble nucleation differently, we also examined TX-100 as another popular surfactant molecule, and the results are summarized in **Figure 3**. A quick comparison of **Figures 2** and **3** reveals quite similar nanobubble dynamics in both SDS and TX-100, i.e., more bubbles were seen in the presence of surfactants, a large hysteresis was observed between the forward and backward scans in both cases, etc. However, a closer examination of the results revealed several distinct differences that may further our understanding of nanobubble formation and growth. First, the SDS concentrations used to observe similar changes in nanobubble detections are roughly ten times greater than those of TX-100 (**Figure 2 & 3**). We attribute this difference to the physical properties of the surfactants (charge, size, CMC, surface activity, etc.). For example, the CMC for TX-100 is nearly 40 times smaller than that of SDS. The greater hydrophobic nature of TX-100 likely influences the extent and strength of adsorption to the gas-liquid interface, and in turn, nanobubble dynamics. The surface tension for 75 µM SDS and 0.75 µM TX-100 is ~68.5 mN•m$^{-1}$ and ~62.5 mN•m$^{-1}$, respectively.[41,42] At lower surfactant concentrations we expect the

surface tension to approach bulk water (72.8 mN•m$^{-1}$). Nonetheless, the unknown shape and size of the surface nanobubbles and extent of surfactant adsorption makes it difficult to estimate the surface tension at the gas-liquid interface. Presumably, the surface tension at the nanobubble surface is drastically different from bulk liquid values.

Additionally, the number of detected nanobubbles decreases at the highest TX-100 concentration, 0.75 µM (**Figure 3B**). This is in stark contrast to the SDS case as the number of bubbles appears to reach a plateau around 50 µM (**Figure 2B**). We hypothesize that this difference is related to the size of the nanobubbles: TX-100 stabilized bubbles become too big to be detected within the evanescent wave. The decaying evanescent wave can be used as a crude "optical ruler".[16] Generally, fluorophores closer to the surface of the electrode will tend to be brighter than fluorophores further from the electrode. **Figure S4** shows raw images of nanobubbles formed under constant potential. SDS stabilized nanobubbles appear to be brighter than TX-100 stabilized nanobubbles. Box-and-whisker plots of fluorophore intensity as a function of SDS concentration reveal that the intensity of labeled nanobubble spots increases with increasing SDS concentration; the opposite is seen in TX-100 **(Figure 4)**. The difference in intensity may be due to a difference in nanobubble size (z-direction). TX-100 nanobubbles appear to be larger than the SDS nanobubbles. It is also important to note that the thickness of the surfactant layer may play a role in the "height" of the bubble. Further investigation is warranted.
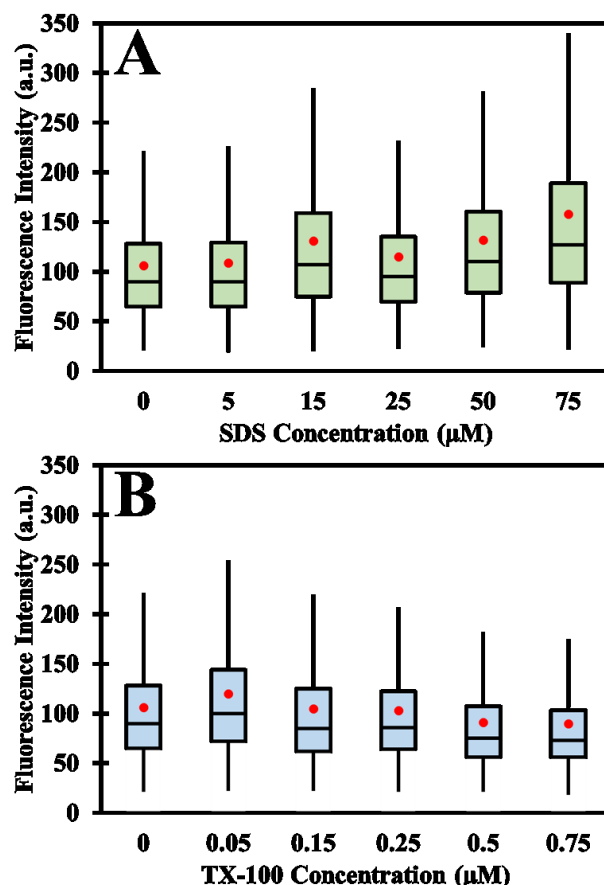
**Figure 4:** Fluorophore intensity as a function of surfactant concentration. -1 V vs Pt QRE constant potential experiment containing 100 pM R6G, 1 M $Na_2SO_4$, and **A)** SDS **B)** TX-100. Each box plot is a collection of 10 experiments with >150,000 detected events per surfactant condition. Outliers 1.5 times the interquartile range were removed. The red circles are average intensities per surfactant concentration.

*Effect of Surfactant on Fluorophore Adsorption.* The kinetics of fluorophore adsorption at the gas-liquid interface changes in the presence of surfactant. Tau ($\tau$), a measure of nanobubble-fluorophore lifetime, is extracted from single exponential decay fitting of histograms of nanobubble lifetimes (**Figure S5**).[16,30] The lifetime of the nanobubble-fluorophore interaction increases roughly from 50 ms without SDS to 70 ms with 15 μM SDS present in solution (**Figure 5A**). The increased lifetime is also immediately apparent from **Video S1**. The accumulation of negatively charged SDS molecules at the gas-liquid interface will produce a greater zeta potential at the surface of the nanobubble. In turn, we propose that the positively charged R6G dye molecules remain on the surface longer due to an increase in electrostatic affinity for the gas-liquid interface. The fluorophore residence time reaches a plateau starting between 15-25 μM. We

believe this indicates that the surface of the nanobubble reaches a saturated level of SDS. A similar saturation concentration (~13 μM) for the cationic surfactant cetrimonium bromide (CTAB) was reported.[15] The difference in the saturation level is likely related to the size of the bubble and to the physical properties of the surfactant.

However, we observe the opposite effect when using TX-100 (non-ionic) (**Figure 4B**). This result is puzzling because it appears that the intensity and residence time of the fluorophore are correlated. If our hypothesis about the intensity trends are correct, the size and shape of nanobubble may also play a role in the adsorption of dye on the nanobubble surface. On the other hand, the hydrophobic nature of TX-100 may lead to a thicker surfactant layer on the bubble surface that results in an unfavorable environment for R6G adsorption. Multiple factors may be at play. A detailed study to explain the change in fluorophore-nanobubble interaction as a function of the gas-liquid interface structure is underway.
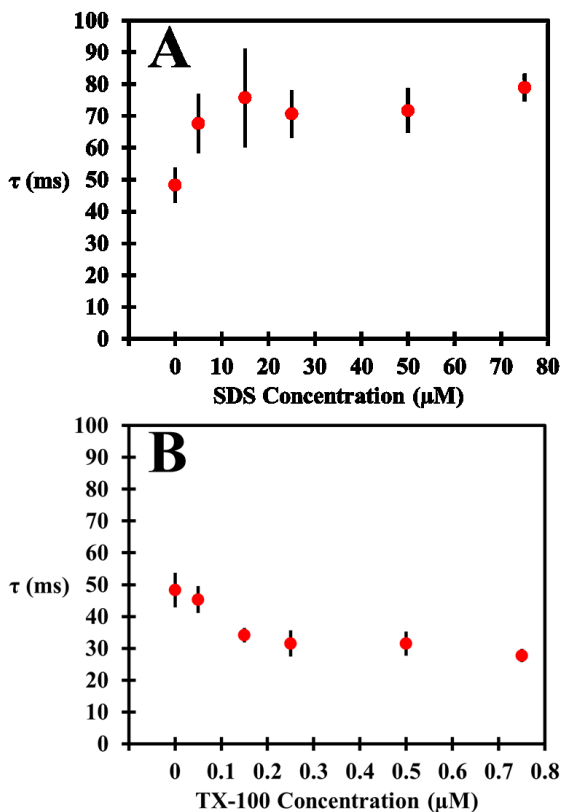


**Figure 5:** Mean fluorophore residence time. -1 V vs Pt QRE constant potential experiment containing 100 pM R6G, 1 M $Na_2SO_4$, and **A)** SDS **B)** TX-100. N=10 for each condition. Error bars represent one standard deviation from the mean.

**Conclusions**

In conclusion, we have used single-molecule fluorescence microscopy as a useful means to study the effect of surfactants on the formation of $H_2$ nanobubbles on the electrode surface. Our results demonstrate that the use of surfactants reduces the potential driving force required to nucleate a nanobubble. This study was successful in probing early nanobubble nucleation before any detectable current change was observed. Additionally, nanobubble production increases in the presence of surfactant across all voltages. We believe that these results can be explained, in part, by a lowering of gas saturation levels needed to nucleate a nanobubble due to a reduction in the surface tension of the gas-water interface. Nevertheless, more work is needed to explain the nucleation of nanobubbles at voltages where an undersaturated environment likely exists. Furthermore, we propose that the rate of nanobubble dissolution decreases as the bubble becomes smaller. A thick surfactant layer may affect the permeability of gas molecules within the nanobubble, which helps the nanobubble stability on the electrode surface.

Finally, we observed changes in fluorophore intensity and residence lifetime in the presence of surfactant. The adsorption of surfactant to the nanobubble surface influences the size and shape of the nanobubble. However, the interaction of the fluorophore with the gas-liquid interface changes as a function of the interface. Currently, we do not fully understand what properties of the bubble (size, shape, etc.) and the surfactant (charge, chain length, hydrophobicity, etc.) impact dye adsorption. Elucidating the major factors influencing the labeling of nanobubbles by dye molecules will provide a better understanding of nanobubble dynamics and the gas-water interface.

**Acknowledgement**

**Associated Content**

*Supporting Information:*

A cyclic voltammogram of Pt in $H_2SO_4$, videos imaging nanobubbles in the presence of SDS and TX-100, control experiment without dye molecules, tentative hypothesis, raw images showing variable intensity for SDS and TX-100, and histogram of fluorophore residence time at the nanobubble surface.

**Notes**

The authors declare no conflict of interest.

**References**

(1) Mallouk, T. E. Divide and Conquer. *Nat. Chem.* **2013**, *5* (5), 362–363. https://doi.org/10.1038/nchem.1634.

(2) Serov, A.; Kwak, C. Direct Hydrazine Fuel Cells: A Review. *Appl. Catal. B Environ.* **2010**, *98* (1–2), 1–9. https://doi.org/10.1016/j.apcatb.2010.05.005.

(3) An, L.; Chen, R. Direct Formate Fuel Cells: A Review. *J. Power Sources* **2016**, *320*, 127–139. https://doi.org/10.1016/j.jpowsour.2016.04.082.

(4) German, S. R.; Edwards, M. A.; Ren, H.; White, H. S. Critical Nuclei Size, Rate, and Activation Energy of H2 Gas Nucleation. *J. Am. Chem. Soc.* **2018**, *140* (11), 4047–4053. https://doi.org/10.1021/jacs.7b13457.

(5) Vogt, H. The Actual Current Density of Gas-Evolving Electrodes - Notes on the Bubble Coverage. *Electrochim. Acta* **2012**, *78*, 183–187. https://doi.org/10.1016/j.electacta.2012.05.124.

(6) Yang, X.; Baczyzmalski, D.; Cierpka, C.; Mutschke, G.; Eckert, K. Marangoni Convection at Electrogenerated Hydrogen Bubbles. *Phys. Chem. Chem. Phys.* **2018**, *20* (17), 11542–11548. https://doi.org/10.1039/c8cp01050a.

(7) Tobias, C. W. Effect of Gas Evolution on Current Distribution and Ohmic Resistance in Electrolyzers. *J. Electrochem. Soc.* **1959**, *106*, 833–837. https://doi.org/10.1007/BF01006856.

(8) Zhao, X.; Ren, H.; Luo, L. Gas Bubbles in Electrochemical Gas Evolution Reactions. *Langmuir* **2019**, *35* (16), 5392–5408. https://doi.org/10.1021/acs.langmuir.9b00119.

(9) German, S. R.; Edwards, M. A.; Chen, Q.; White, H. S. Laplace Pressure of Individual H2 Nanobubbles from Pressure-Addition Electrochemistry. *Nano Lett.* **2016**, *16* (10), 6691–6694. https://doi.org/10.1021/acs.nanolett.6b03590.

(10) Zhang, X. H.; Quinn, A.; Ducker, W. A. Nanobubbles at the Interface between Water and a Hydrophobic Solid. *Langmuir* **2008**, *24* (9), 4756–4764. https://doi.org/10.1021/la703475q.

(11) Liu, Y.; Zhang, X. Nanobubble Stability Induced by Contact Line Pinning. *J. Chem. Phys.* **2013**, *138*, 014706. https://doi.org/10.1063/1.4773249.

(12) Liu, Y.; Edwards, M. A.; German, S. R.; Chen, Q.; White, H. S. The Dynamic Steady State of an Electrochemically Generated Nanobubble. *Langmuir* **2017**, *33* (8), 1845–1853. https://doi.org/10.1021/acs.langmuir.6b04607.

(13) Ducker, W. A. Contact Angle and Stability of Interfacial Nanobubbles. *Langmuir* **2009**, *25* (16), 8907–8910. https://doi.org/10.1021/la902011v.

(14) Das, S. Effect of Impurities in the Description of Surface Nanobubbles: Role of Nonidealities in the Surface Layer. *Phys. Rev. E - Stat. Nonlinear, Soft Matter Phys.* **2011**, *83* (6), 1–14. https://doi.org/10.1103/PhysRevE.83.066315.

(15) Chen, Q.; Luo, L.; Faraji, H.; Feldberg, S. W.; White, H. S. Electrochemical Measurements of Single H2 Nanobubble Nucleation and Stability at Pt Nanoelectrodes. *J. Phys. Chem. Lett.* **2014**, *5*

(20), 3539–3544. https://doi.org/10.1021/jz501898r.

(16) Hao, R.; Fan, Y.; Howard, M. D.; Vaughan, J. C.; Zhang, B. Imaging Nanobubble Nucleation and Hydrogen Spillover during Electrocatalytic Water Splitting. *Proc. Natl. Acad. Sci.* **2018**, *115* (23), 5878–5883. https://doi.org/10.1073/pnas.1800945115.

(17) Hao, R.; Fan, Y.; Anderson, T. J.; Zhang, B. Imaging Single Nanobubbles of H2 and O2 during the Overall Water Electrolysis with Single-Molecule Fluorescence Microscopy. *Anal. Chem.* **2020**, *92* (5), 3682–3688. https://doi.org/10.1021/acs.analchem.9b04793.

(18) Zhang, L.; Zhang, Y.; Zhang, X.; Li, Z.; Shen, G.; Ye, M.; Fan, C.; Fang, H.; Hu, J. Electrochemically Controlled Formation and Growth of Hydrogen Nanobubbles. **2006**, No. 6, 8109–8113. https://doi.org/10.1021/la060859f.

(19) Ma, Y.; Highsmith, A. L.; Hill, C. M.; Pan, S. Dark-Field Scattering Spectroelectrochemistry Analysis of Hydrazine Oxidation at Au Nanoparticle-Modified Transparent Electrodes. *J. Phys. Chem. C* **2018**, *122* (32), 18603–18614. https://doi.org/10.1021/acs.jpcc.8b05112.

(20) Zhao, X.; Ranaweera, R.; Mixdorf, J. C.; Nguyen, H. M.; Luo, L. Lowering Interfacial Dissolved Gas Concentration for Highly Efficient Hydrazine Oxidation at Platinum by Fluorosurfactant Modulation. *ChemElectroChem* **2020**, *7*, 55–58. https://doi.org/10.1002/celc.201901781.

(21) Chan, C. U.; Ohl, C. D. Total-Internal-Reflection-Fluorescence Microscopy for the Study of Nanobubble Dynamics. *Phys. Rev. Lett.* **2012**, *109* (17), 1–5. https://doi.org/10.1103/PhysRevLett.109.174501.

(22) Su, H.; Fang, Y.; Chen, F.; Wang, W. Monitoring the Dynamic Photocatalytic Activity of Single CdS Nanoparticles by Lighting up H2 Nanobubbles with Fluorescent Dyes. *Chem. Sci.* **2018**, *9* (6), 1448–1453. https://doi.org/10.1039/c7sc04684g.

(23) Perez Sirkin, Y. A.; Gadea, E. D.; Scherlis, D. A.; Molinero, V. Mechanisms of Nucleation and Stationary States of Electrochemically Generated Nanobubbles. *J. Am. Chem. Soc.* **2019**, jacs.9b04479. https://doi.org/10.1021/jacs.9b04479.

(24) Edwards, M. A.; White, H. S.; Ren, H. Voltammetric Determination of the Stochastic Formation Rate and Geometry of Individual $H_2$, $N_2$ , and $O_2$ Bubble Nuclei. *ACS Nano* **2019**, *13*, acsnano.9b01015. https://doi.org/10.1021/acsnano.9b01015.

(25) Ovesný, M.; Křížek, P.; Borkovec, J.; Švindrych, Z.; Hagen, G. M. ThunderSTORM: A Comprehensive ImageJ Plug-in for PALM and STORM Data Analysis and Super-Resolution Imaging. *Bioinformatics* **2014**, *30* (16), 2389–2390. https://doi.org/10.1093/bioinformatics/btu202.

(26) Tinevez, J. Y.; Perry, N.; Schindelin, J.; Hoopes, G. M.; Reynolds, G. D.; Laplantine, E.; Bednarek, S. Y.; Shorte, S. L.; Eliceiri, K. W. TrackMate: An Open and Extensible Platform for Single-Particle Tracking. *Methods* **2017**, *115*, 80–90. https://doi.org/10.1016/j.ymeth.2016.09.016.

(27) Alsabet, M.; Grden, M.; Jerkiewicz, G. Comprehensive Study of the Growth of Thin Oxide Layers on Pt Electrodes under Well-Defined Temperature, Potential, and Time Conditions. *J. Electroanal. Chem.* **2006**, *589* (1), 120–127. https://doi.org/10.1016/j.jelechem.2006.01.022.

(28) Parsons, R.; Visscher, W. H. M. An Ellipsometric Investigation of Adsorbed Layers on Platinum Electrodes at High Anodic Potentials. *J. Electroanal. Chem.* **1972**, *36* (2), 329–336. https://doi.org/10.1016/S0022-0728(72)80255-9.

(29) Biegler, T.; Woods, R. Limiting Oxygen Coverage on Smooth Platinum Anodes in Acid Solution. *J. Electroanal. Chem.* **1969**, *20* (1), 73–78. https://doi.org/10.1016/0368-1874(89)80007-3.

(30)   Lu, J.; Fan, Y.; Howard, M. D.; Vaughan, J. C.; Zhang, B. Single-Molecule Electrochemistry on a Porous Silica-Coated Electrode. *J. Am. Chem. Soc.* **2017**. https://doi.org/10.1021/jacs.6b10191.

(31)   Mukerjee, P.; Mysels, K. J. *Critical Micelle Concentrations of Aqueous Surfactant Systems*; National Standard Reference Data System, 1971.

(32)   Lubetkin, S.; Blackwell, M. The Nucleation of Bubbles in Supersaturated Solutions. *J. Colloid Interface Sci.* **1988**, *126* (2), 610–615. https://doi.org/10.1016/0021-9797(88)90161-0.

(33)   Zhang, X.; Jackson, J. K.; Burt, H. M. Determination of Surfactant Critical Micelle Concentration by a Novel Fluorescence Depolarization Technique. *J. Biochem. Biophys. Methods* **1996**, *31* (3–4), 145–150. https://doi.org/10.1016/0165-022X(95)00032-M.

(34)   Zhao, X.; Ranaweera, R.; Luo, L. Highly Efficient Hydrogen Evolution of Platinum: Via Tuning the Interfacial Dissolved-Gas Concentration. *Chem. Commun.* **2019**, *55* (10), 1378–1381. https://doi.org/10.1039/c8cc08803a.

(35)   German, S. R.; Edwards, M. A.; Chen, Q.; Liu, Y.; Luo, L.; White, H. S. Electrochemistry of Single Nanobubbles. Estimating the Critical Size of Bubble-Forming Nuclei for Gas-Evolving Electrode Reactions. *Faraday Discuss.* **2016**, *193*, 223–240. https://doi.org/10.1039/c6fd00099a.

(36)   Soto, Á. M.; German, S. R.; Ren, H.; Van Der Meer, D.; Lohse, D.; Edwards, M. A.; White, H. S. The Nucleation Rate of Single O2 Nanobubbles at Pt Nanoelectrodes. *Langmuir* **2018**, *34* (25), 7309–7318. https://doi.org/10.1021/acs.langmuir.8b01372.

(37)   Seddon, J. R. T.; Kooij, E. S.; Poelsema, B.; Zandvliet, H. J. W.; Lohse, D. Surface Bubble Nucleation Stability. *Phys. Rev. Lett.* **2011**, *106*, 056101. https://doi.org/10.1103/PhysRevLett.106.056101.

(38)   Hanwright, J.; Zhou, J.; Evans, G. M.; Galvin, K. P. Influence of Surfactant on Gas Bubble Stability. *Langmuir* **2005**, *21* (11), 4912–4920. https://doi.org/10.1021/la0502894.

(39)   German, S. R.; Wu, X.; An, H.; Craig, V. S. J.; Mega, T. L.; Zhang, X. Interfacial Nanobubbles Are Leaky: Permeability of the Gas/Water Interface. *ACS Nano* **2014**, *8* (6), 6193–6201. https://doi.org/10.1021/nn5016049.

(40)   Guo, Z.; Wang, X.; Zhang, X. Stability of Surface Nanobubbles without Contact Line Pinning. *Langmuir* **2019**, *35*, 8482–8489. https://doi.org/10.1021/acs.langmuir.9b00772.

(41)   Hernainz-Bermudez De Castro, F.; Gálvez-Borrego, A.; Calero-de Hoces, M. Surface Tension of Aqueous Solutions of Sodium Dodecyl Sulfate from 20 °C to 50 °C and PH between 4 and 12. *J. Chem. Eng. Data* **1998**, *43* (5), 717–718. https://doi.org/10.1021/je9800149.

(42)   Bzdek, B. R.; Reid, J. P.; Malila, J.; Prisle, N. L. The Surface Tension of Surfactant-Containing, Finite Volume Droplets. *Proc. Natl. Acad. Sci. U. S. A.* **2020**, *117* (15), 8335–8343. https://doi.org/10.1073/pnas.1915660117.

Table of Contents Figure